AGU PUBLICATIONS

Geophysical Research Letters

RESEARCH LETTER
10.1002/2015GL067014

Key Points:
- Typical and long recovery VLF scattering events are explained by a self-consistent chemistry model
- VLF recovery timescales are quantitatively estimated from the modeled electron density enhancements
- The physical mechanisms explaining LOREs are not exclusive to EMP heating (i.e., elves)

Supporting Information:
- Table S1

Correspondence to:
D. A. Kotovsky,
dakotovsky@ufl.edu

Citation:
Kotovsky, D. A., and R. C. Moore (2016), Photochemical response of the nighttime mesosphere to electric field heating—Recovery of electron density enhancements, *Geophys. Res. Lett.*, *43*, 952–960, doi:10.1002/2015GL067014.

Received 13 NOV 2015
Accepted 8 JAN 2016
Accepted article online 15 JAN 2016
Published online 4 FEB 2016

Photochemical response of the nighttime mesosphere to electric field heating—Recovery of electron density enhancements

D. A. Kotovsky[1] and R. C. Moore[1]

[1]Department of Electrical and Computer Engineering, University of Florida, Gainesville, Florida, USA

Abstract A photochemical model has been developed to examine the response of the nighttime mesosphere to electric field heating. Time dynamics of 29 chemical species are accounted for by a set of 156 reactions. Recovery dynamics of electron density enhancements are examined in detail, and the recovery timescales of VLF scattering resulting from the modeled conductivity changes are quantitatively estimated. Both typical recovery (up to 240 s) and long recovery (>300 s) timescales of early VLF scattering events are explainable in terms of the model results. Electron production and loss during recovery is determined by a small set of attachment, detachment, and recombination processes. Based on the model results, we conclude that long recovery VLF scattering proceeds from sufficiently large electron density enhancements that are controlled by slow recombination loss (i.e., when attachment loss is small or balanced by detachment).

1. Introduction

Electric field intensity changes produced by lightning discharges are capable of directly ionizing the mesosphere (~50 km up to ~100 km altitude), sometimes resulting in the scattering of subionospherically propagating very low frequency (VLF, 3–30 kHz) waves [e.g., *Inan et al.*, 1996; *Dowden et al.*, 1997; *Hardman et al.*, 1998; *Haldoupis et al.*, 2006, 2010; *Marshall et al.*, 2006, 2014; *Cheng et al.*, 2007]. Recently, a class of these "early VLF" scattering events was identified which exhibit recoveries up to tens of minutes [*Cotts and Inan*, 2007], much longer than typical recoveries of 60–240 s (onset to zero pertubation) [*Sampath et al.*, 2000]. Various atmospheric chemistry models have been developed that explain the typical recoveries of lightning-induced VLF perturbations [e.g., *Pasko and Inan*, 1994; *Nunn and Rodger*, 1999; *Haldoupis et al.*, 2009]. However, attempts to explain long recovery, early VLF events (LOREs, >300 s recovery) have heretofore been unsuccessful.

Possible association of LOREs with long lasting, stratospheric ion enhancements produced by gigantic jets was suggested by *Cotts and Inan* [2007]; however, the gigantic jet-produced conductivity changes modeled by *Lehtinen and Inan* [2007] were too small to produce observable VLF scattering. Noting that electron lifetimes increase as the total electron density decreases, *Cotts and Inan* [2007] and *Haldoupis et al.* [2009] suggested that LOREs might be associated with small electron density enhancements of a tenuous ionosphere. From our model results, we find that electron lifetimes in the upper mesosphere are long at the end of most ionization events, and thus, more is needed to explain LORE observations and their relative rarity (i.e., analysis of plasma refractive index). Further, as noted by *Liu* [2012] and discussed in section 2.2 in this paper, simple negative ion groupings such as those used by *Haldoupis et al.* [2009] inevitably lead to inaccuracies when applied to the nighttime mesosphere. It is uncertain how seriously these inaccuracies affect modeled electron recovery times.

Modeling the cumulative ionization due to thunderstorm electromagnetic radiation, *Rodger et al.* [2001] noted that modeled electron density enhancements, occurring above 85 km, exhibited long recovery times due to slow recombination loss. *Rodger* [2003] and *Haldoupis et al.* [2012, 2013] reference the quantitative analysis of *Rodger et al.* [2001] to argue that LOREs are explained by conductivity changes associated with elves occurring at or above 85 km and near nighttime VLF reflection heights. Recent experimental analyses estimate that typical nighttime VLF reflection heights [i.e., h' of the Wait and Spies profile *Wait and Spies*, 1964] are around 85±1 km [e.g., *Thomson et al.*, 2007; *Thomson and McRae*, 2009; *Han and Cummer*, 2010], indicating

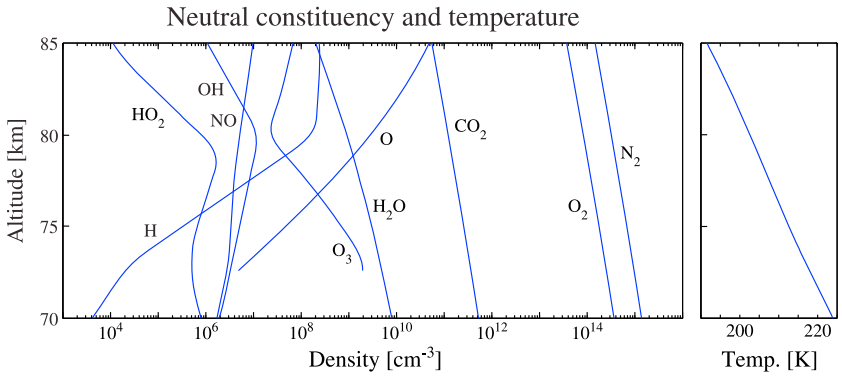

Figure 1. Neutral constituency and temperature.

that VLF radio waves are generally not sensitive to conductivity changes above ~85 km. This work will demonstrate that long recovery VLF scattering (due also to slow recombination loss) can occur below 80 km, well beneath nighttime VLF reflection heights. Consequently, LOREs do not need to be explained by ionospheric disturbances occurring only above 85 km nor must LOREs be specifically associated with elves.

Detailed sprite chemistry modeling at 70 km, including analysis of electron dynamics, has been presented by *Sentman et al.* [2008]. *Gordillo-Vázquez* [2008, 2010] and *Gordillo-Vázquez and Luque* [2010] present similar sprite chemistry modeling up to 80 km but did not include hydrated positive ion clusters which significantly reduce electron lifetimes in the upper mesosphere (see section 2.2 of this work). *Enell et al.* [2008] have modeled the effects of lightning electric field heating on mesospheric ozone and odd nitrogen species; they did not, however, present analysis of electron or ion dynamics.

The quantitative analysis of electron density and conductivity recoveries which can explain long recovery VLF scattering, utilizing a chemistry model that properly accounts for electron and ion dynamics, to our knowledge, is absent in the current literature. We note that although the works of *Sentman et al.* [2008] and *Enell et al.* [2008] did not present analysis of electron enhancements exhibiting long recoveries, the chemistry models used in those works do contain the essential processes that explain long recovery VLF scattering.

In this paper, we present results from a photochemical model of the nighttime mesosphere, accounting for the dynamics of electrons, 10 neutral species, 11 negative ion species, 6 positive ion species, and 1 grouping of positive ion clusters. Dynamics of electron and ion density changes between 75 and 80 km in response to Gaussian-shaped electric field heating pulses are examined. Physical mechanisms leading to both typical recovery and long recovery VLF events are explained.

2. Description of the Model

The photochemical model used in this work is largely based upon the models of *Rowe et al.* [1974], *Thomas and Bowman* [1985], and *Sentman et al.* [2008]. In the following, we will describe only the essential parts of the model. A more fully detailed description of the model will be provided in a forthcoming paper.

Time dynamics of 29 species [$N_2(A)$, $N_2(B)$, $N_2(a')$, $N_2(C)$, $N(^4S)$, N*, $O_2(a)$, $O_2(b)$, NO, NO_2, e^-, O^-, O_2^-, O_3^-, O_4^-, OH^-, CO_3^-, CO_4^-, NO_2^-, NO_3^-, $O_2^-{\cdot}NO$, HCO_3^-, N_2^+, N^+, O_2^+, O^+, O_4^+, NO^+, and Y^+] are accounted for by a set of 156 reactions (see Table S1 in the supporting information). N* is a grouping of electronically excited atomic nitrogen, and Y^+ is a grouping of positive ion clusters. Densities of nine neutral species [N_2, O_2, O, O_3, H_2O, H, OH, HO_2, and CO_2] are taken to be constant throughout the simulation (shown in Figure 1). Concentrations of N_2, O_2, and O and a neutral temperature (T_n) profile are obtained from the NRLMSISE-00 model [*Picone et al.*, 2002] for nighttime summer conditions. Densities of H, OH, and HO_2 are adopted from the midnight calculations of *Allen et al.* [1984]. The mixing ratio of H_2O is adopted from *Brasseur and Solomon* [2005, pp. 617]. For the conditions modeled, the net amount of atomic oxygen produced during electric field heating is negligible compared to its ambient density—we thereby take the density of atomic oxygen to be constant. Ozone density is calculated by the steady state balance of reactions R157 through R162 (see Table S1 for reaction set). We assume a uniform CO_2 mixing ratio of 300 ppm.

Calculations are performed at individual altitudes independent of all other altitudes. Thus, transport processes such as molecular, eddy, and ambipolar diffusion are excluded. Loss of electrons and ions via ambipolar diffusion in the ambient ionosphere is negligible below 150 km [*Whitten and Poppoff*, 1965, pp. 125] but may become important when electron or ion density gradients are sufficiently large (e.g., for sprite or gigantic jet columns). Molecular and eddy diffusion significantly impact odd nitrogen (N, NO, and NO_2) [e.g., *Strobel et al.*, 1970; *Sentman et al.*, 2008]; thereby, exclusion of transport processes does not allow for full calculation of odd nitrogen enhancement recoveries.

Ambient sources of ionization included in the model are galactic cosmic rays (GCR, R1 – R7 in reaction set) and solar Lyman β (R8) and Lyman α (R9). Ion pair production rates due to galactic cosmic rays (GCR) are calculated using the parametrization of *Heaps* [1978], for a magnetic latitude of 35° during solar maximum. The incident fluxes of Lyman β and Lyman α at 220 km are taken to be 30 R (rayleigh, 1 R = 10^6 photons cm^{-2} s^{-1}) for Lyman β and 5 kR for Lyman α, corresponding to a solar zenith angle near 120° [*Meier*, 1969; *Meier and Mange*, 1973]. Flux reaching lower altitudes is determined by absorption via molecular oxygen. The absorption cross sections of O_2 for Lyman β and Lyman α are taken to be 1.55×10^{-18} cm^2 and 1.04×10^{-22} cm^2, respectively [*Watanabe*, 1958]. The ionization cross section of O_2 for Lyman β is taken to be 0.90×10^{-18} cm^2, and the ionization cross section of NO for Lyman α is taken to be 2.02×10^{-18} cm^2.

Without sufficient information available to calculate positive ion cluster composition and dynamics, all positive ion clusters are grouped together as a single constituent [Y^+]. Production of Y^+ proceeds through the initial hydration steps of O_4^+ and NO^+. Details regarding the hydration of NO^+ are uncertain [e.g., *Reid*, 1977; *Arnold et al.*, 1980]. We thereby adopt the empirical rate of NO^+ hydration from *Arnold et al.* [1980]. The electron-ion recombination rate coefficient for Y^+ is taken to be that of hydronium water clusters, $H_3O^+ \cdot (H_2O)_n$, for a cluster order $n = 3$, corresponding to a moderately wet and cold, summertime mesosphere [*Reid*, 1977]. Details of negative ion dynamics are discussed in section 2.1. The generalized ion-ion recombination rate coefficient (R113) of *Smith and Church* [1977] is adopted. Three-body ion-ion processes, important only below 30 km [*Smith and Church*, 1977], are excluded.

The quasi-equilibrium composition of the 29 dynamic species is found by iteratively solving the photochemical continuity equations until the production and loss rates of each species agree to within 1%. An additional, ambient 2 h simulation is run ensuring that species densities change by no more than 1%. Determination of the quasi-equilibrium density of nitric oxide is an exception. Due to its long lifetime, nighttime concentrations of nitric oxide in the mesosphere are determined by its daytime production [*Ogawa and Shimazaki*, 1975]. We therefore adopt the quasi-equilibrium density of NO from the diurnal calculations of *Ogawa and Shimazaki* [1975].

2.1. Electron Attachment, Detachment, and Negative Ion Conversion Processes

With the absence of photodetachment during nighttime (see discussion in *Mitra* [1975]), the loss mechanisms for dominant negative ions [CO_3^-, NO_3^-, and HCO_3^-] are (1) conversion to simpler ions (R69 for CO_3^- and R80 for NO_3^-) or (2) slow ion-ion recombination (R113 for HCO_3^-). Equilibrium densities of these dominant ions depend significantly upon the densities of the minor constituent ions from which they are produced (O_3^-, NO_2^-, and OH^-, respectively). Minor constituent densities are in turn sensitive to reactions which reconvert complex ions to simple ions (e.g., R51, R56, R62, R68, and R80). As a result, negative ion composition in the nighttime upper mesosphere is highly interdependent.

Due to the sharp increase of atomic oxygen and decrease in O_2 and O_3 with increasing altitude, negative ion composition undergoes a significant change in the nighttime upper mesosphere. The ambient electron densities and negative ion composition of our simulations is shown in Table 1, which agree well with the modeling results of *Thomas and Bowman* [1985]. As a result of the diverse negative ion composition and the strong interdependence of negative ion species, we found that no simple groupings of negative ions for the nighttime mesosphere were achievable without introducing significant inaccuracies. The negative ion scheme of *Thomas and Bowman* [1985] is therefore adopted. Three-body attachment and detachment processes are negligible for the altitudes considered here (above 75 km) and are excluded.

Because no "effective" negative ion loss rate accurately represents conditions throughout the nighttime upper mesosphere, it is difficult to assess the error in electron recovery calculations introduced by simple negative ion grouping. Previous models [e.g., *Gluhkov et al.*, 1992; *Haldoupis et al.*, 2009] have utilized effective negative ion detachment rates which correspond to effective *daytime* detachment rates [*Rowe et al.*, 1974; *Mitra*,

Table 1. Ambient Negative Ion Composition (Altitude in km, Densities in cm^{-3})[a]

Altitude	e^-	O^-	O_2^-	O_3^-	O_4^-	OH^-	CO_3^-	CO_4^-	NO_2^-	NO_3^-	$O_2^-\cdot NO$	HCO_3^-	$\sum N_x^+$	λ
75	3.56 (−1)	7.35 (−2)	7.23	1.12	4.94 (−3)	1.07 (−2)	1.48 (2)	6.25	1.31	1.98 (2)	3.94 (−4)	5.97 (1)	4.22 (2)	1.18 (3)
76	2.01	4.00 (−1)	1.23 (1)	6.41 (−1)	7.27 (−3)	3.94 (−2)	8.42 (1)	1.22 (1)	2.34	8.48 (1)	9.46 (−4)	1.80 (2)	3.79 (2)	1.87 (2)
77	5.96	7.66 (−1)	8.13	1.58 (−1)	4.17 (−3)	5.24 (−2)	2.05 (1)	6.07	4.98 (−1)	4.02	5.77 (−4)	2.38 (2)	2.84 (2)	4.66 (1)
78	1.22 (1)	8.75 (−1)	3.63	3.12 (−2)	1.61 (−3)	3.89 (−2)	3.94	1.25	3.41 (−2)	5.91 (−2)	1.48 (−4)	1.81 (2)	2.03 (2)	1.57 (1)
79	2.46 (1)	8.43 (−1)	1.67	7.37 (−3)	6.34 (−4)	2.03 (−2)	8.44 (−1)	2.08 (−1)	2.44 (−3)	9.00 (−4)	3.19 (−5)	1.05 (2)	1.34 (2)	4.43
80	4.55 (1)	7.53 (−1)	9.06 (−1)	2.39 (−3)	2.96 (−4)	7.64 (−3)	2.20 (−1)	4.02 (−2)	2.79 (−4)	3.02 (−5)	7.85 (−6)	4.28 (1)	9.02 (1)	9.83 (−1)

[a] $\sum N_x^+$ is the total positive ion density, and λ is the ratio of negative ions to electrons. Numbers in parenthesis denote factors of ten (e.g., $5.6(-3) = 5.6 \times 10^{-3}$).

1975], which include photodetachment processes that control complex negative ion loss and equilibrium composition.

2.2. Electron Impact Processes

The electric field heating scheme used is largely adopted from *Sentman et al.* [2008]. At the beginning of each simulation, an electric field is applied at altitude with a Gaussian waveshape described by $E(t) = E_o \exp(-t^2/\Delta t^2)$, where E_o is the peak electric field and Δt is the "1/*e*" half width. For the simulations shown, $\Delta t = 10\mu s$, and E_o varies from $2E_k$ to $5E_k$, where E_k is the conventional breakdown field, taken here to be $M\times$ 123 Townsend, where M is the total gas density (cm^{-3}) and 1 Townsend = 10^{-17} V cm^2. The Gaussian pulse is chosen for convenience, in order to identify the important processes controlling electron recovery, and is not intended to replicate actual electric field changes in the *D* region ionosphere produced by lightning discharges. The mean electron temperature, T_e (eV), during heating is determined from the piecewise model of *Sentman et al.* [2008], and the minimum electron temperature is set to the neutral temperature.

Estimates of electron temperatures, utilizing optical measurements, range from 1 to 10 eV in sprites [*Sentman et al.*, 2008, section 4.3] and from 2 to 6 eV in sprite halos [*Miyasato et al.*, 2003]. Given that LOREs are often associated with large peak current flashes, sometimes >200 kA [e.g., *Haldoupis et al.*, 2013; *Salut et al.*, 2013], the electron temperatures modeled in this work (up to ~7.5 eV for $E_o = 5E_k$) are not unrealistic.

Simulations are run independently every 1 km between 75 and 80 km. The density of each of the 29 dynamic species is updated at each time step of the simulation (time steps vary from 10 ns during the heating pulse to 100 μs during recovery) by solving the photochemical continuity equation using a first-order accurate forward finite-difference scheme. Each model run is calculated out to 1 h of simulated time.

3. Recovery Timescales of VLF Scattering

The past works of *Rodger* [2003], *Cotts and Inan* [2007], and *Haldoupis et al.* [2009, 2012, 2013] have considered only the recovery timescales of electron density enhancements and have not analyzed the timescales for which those electron density enhancements are large enough to produce observable VLF scattering. Consequently, we compare our modeled electron densities ($[e^-]$) to an altitude-dependent reference electron density ($[e^-]_{ref}$) at which point the local plasma transitions from a weakly conducting dielectric ($[e^-]<[e^-]_{ref}$) to a good conductor ($[e^-]>[e^-]_{ref}$) at VLF frequencies. This transition occurs approximately when the complex relative permittivity, $\hat{\epsilon}_r = 1 + (i/\omega\epsilon_o)\hat{\sigma}_{||} = 1 + (i/\omega)[\omega_p^2/(\nu - i\omega)]$, has equal real and imaginary parts, where ω is the wave frequency, $\sigma_{||}$ is the parallel conductivity, ω_p is the plasma frequency, and ν is the effective electron collision frequency. Since electron temperatures recover quickly in the *D* region (milliseconds or less), the effective electron collision frequency is calculated for $T_e = T_n$: $\nu = 3.7 \times 10^{-9}(T_n/300)^{1/2}\ M\ s^{-1}$ [*Ratcliffe*, 1959, pp. 32].

We have separately calculated the Appleton-Hartree solutions for the refractive index (for an electron gyrofrequency $\omega_B = 2\pi\times$1.25 MHz), which show that both refractive index solutions deviate from 1 only when $[e^-]$ is near to or greater than $[e^-]_{ref}$. Thus, when $[e^-]>[e^-]_{ref}$s, the local plasma is an efficient VLF scattering body. When $[e^-]\ll[e^-]_{ref}$, VLF radio waves will be only weakly scattered or not scattered at all.

In the ambient lower ionosphere, the altitude where the plasma transitions to a good VLF conductor (i.e., $[e^-]_o \simeq [e^-]_{ref}$) acts as the effective VLF reflection height [*Ratcliffe*, 1959, pp. 32], meaning that most of the VLF wave will have been reflected upon reaching this altitude. For the conditions modeled in this paper, the

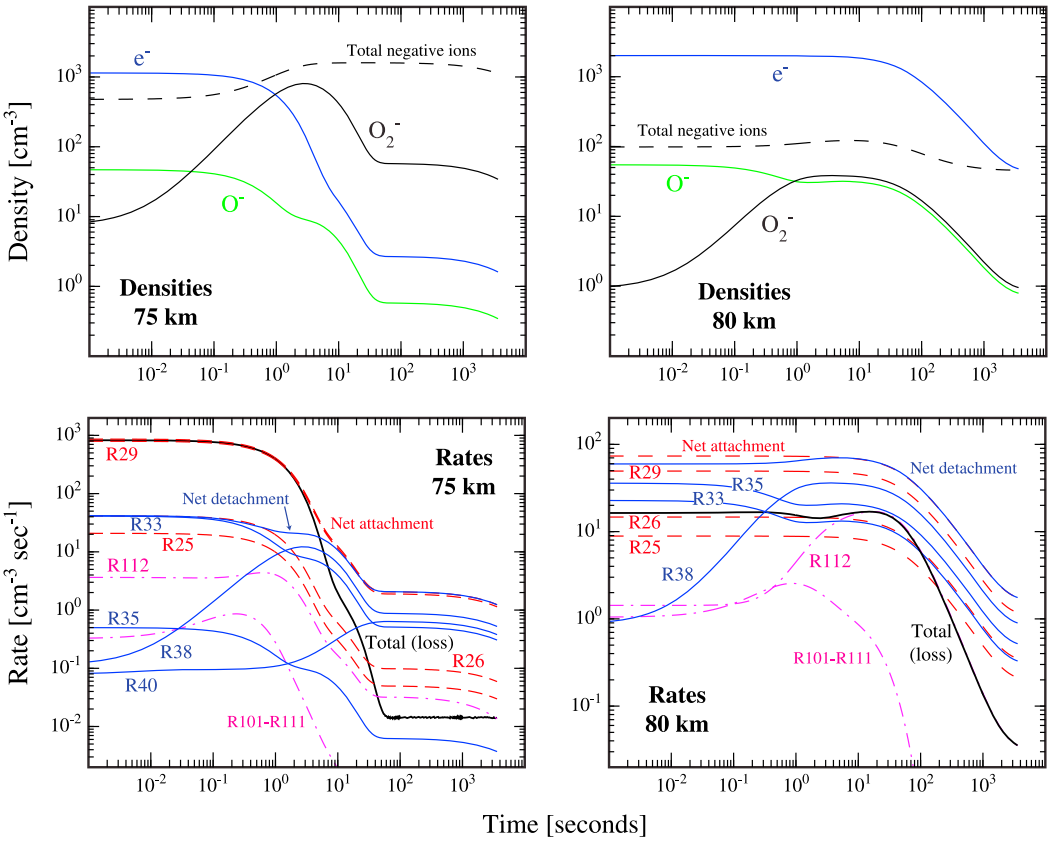

Figure 2. (top row) Electron (blue), O^- (green), O_2^- (solid black), and the total negative ion (dashed black) densities at 75 and 80 km for $E_o = 4E_k$. (bottom row) Corresponding attachment (dashed), detachment (solid blue), recombination (dash-dotted magenta), and total electron loss (solid black) rates.

ambient effective VLF reflection height is around 82 km, indicating that the modeled conductivity changes (typical recovery and long recovery) occurring at and below 80 km will be sensed by VLF radio waves.

4. Results

The following discussion will make continual reference to the results shown in Figures 2 and 3. Detailed electron production and loss rates at 75 and 80 km for $E_o = 4E_k$ are shown in the bottom row of Figure 2, and the corresponding electron, O^-, O_2^-, and total negative ion densities shown in the top row of Figure 2. Shown in Figure 3 are the modeled electron densities during the recovery stage at each altitude for the independent simulations $E_o = 2E_k$, $3E_k$, $4E_k$, or $5E_k$ (note that E_k is an altitude-dependent quantity). Also included in Figure 3 are the ambient electron densities ($[e^-]_o$, blue dashed lines) and a range of reference electron densities at each altitude corresponding to wave frequencies ranging from 20 to 40 kHz ($[e^-]_{ref}$, red shaded area)—note that lower wave frequencies correspond to lower reference electron densities (i.e., bottom of the red shade corresponds to 20 kHz, and top corresponds to 40 kHz).

At 75 km, electrons dissociatively attach with ozone to produce O_2^- (R29), leading to rapid initial recoveries of the electron density enhancements. O^- production occurs predominantly during the heating pulse via reactions R24 and R27. Ion-atom interchange of O_2^- with atomic oxygen (R51) provides an additional source of O^-. Ion conversion of O_2^- to more complex ions proceeds through O_3^- (R52) and O_4^- (R53). Electron attachment processes continue to dominate the net electron loss rate until enough O_2^- is produced such that the combined detachment rates of O^- (R33), O_2^- (R38), and O_3^- (R40) balance the total attachment rate (dominated by R29). Subsequent electron loss rate is then controlled by slower electron-ion recombination with positive cluster ions (R112), offset slightly by residual negative ion detachment. The transition from attachment-dominated loss to recombination-dominated loss can be seen in the change in slope of the electron recoveries of Figures 2 and 3.

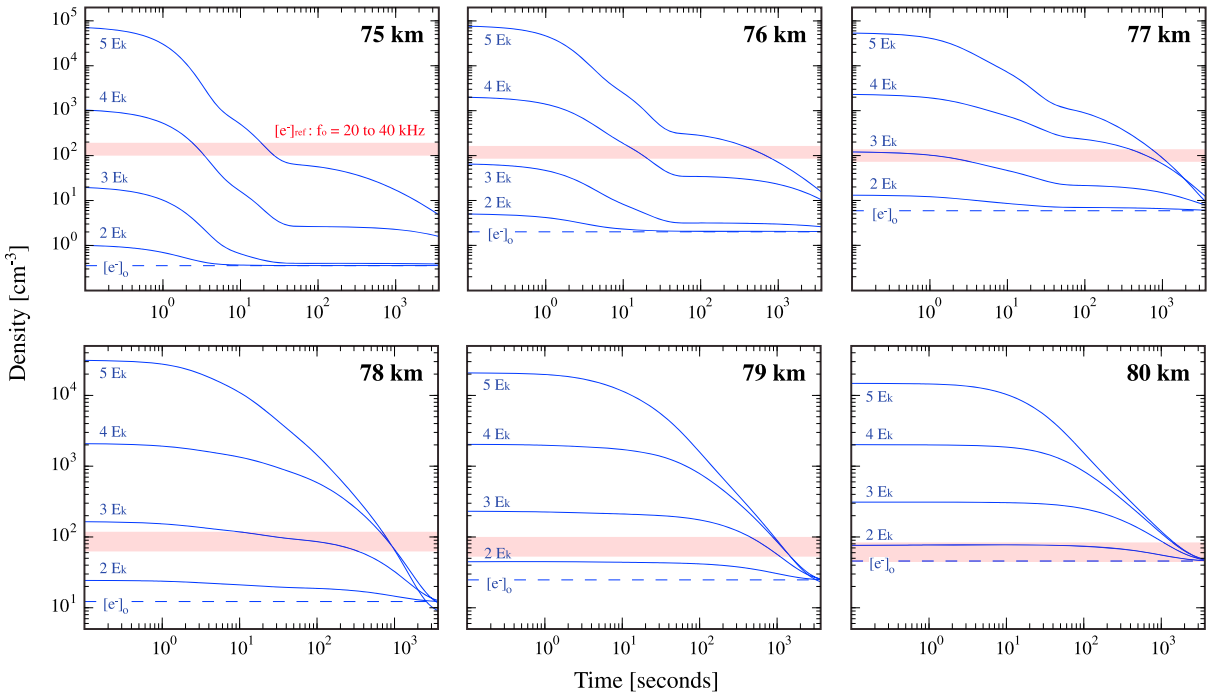

Figure 3. Electron densities in response to electric field heating (solid blue), the quasi-equilibrium electron density (dashed blue), and a range of reference electron densities corresponding to wave frequencies from 20 to 40 kHz (red shaded area, see text for description). Note that simulations were run independently at each altitude and that E_k is an altitude-dependent quantity.

With increasing altitude, attachment rates decrease due to the diminishing concentrations of O_2 and ozone; meanwhile, detachment rates increase due to the increasing concentration of atomic oxygen. As a result, with increasing altitude the total loss rate of electrons via attachment decreases, and less time is required for detachment rates to balance out attachment rates. Consequently, fewer electrons are converted into negative ions, and electron density enhancements remaining after detachment and attachment processes balance become subject to the much slower loss rates of electron-ion recombination. For the conditions modeled, positive ions produced during the heating pulse are converted into positive ion clusters (Y^+) within tens of seconds, such that the total recombination rate is dominated by recombination with cluster ions (R112). Though much larger than recombination rates with simple positive ions, R112 is significantly slower than attachment processes which dominate in the earlier recovery stages at lower altitudes.

Due to the decreasing electron loss rates with increasing altitude, electron density enhancements at higher altitudes persist above the $[e^-]_{ref}$ levels for longer times. At 80 km, where the electron loss rate is almost entirely controlled by recombination (R112), the enhanced electron densities exceed $[e^-]_{ref}$ for >1000 s. In contrast, at 75 km the electron densities decreased to values below $[e^-]_{ref}$ within 30 s. We note that the time required for the electrons to recover to the $[e^-]_{ref}$ level depends not only on altitude but also upon the strength of the modeled electric field heating pulse. Variation in the electron density recovery times as a function of the electric field heating pulse magnitude is most clearly visible for the model runs performed at 77 km, where the time it takes for the enhanced electron density to recover to $[e^-]_{ref}$ varies from ~2 s ($E_o = 3E_k$) to ~1000 s ($E_o = 5E_k$).

5. Discussion

The dominant factors which control the photochemical lifetimes of electrons are (1) the strengths of attachment and detachment processes, dependent upon the composition of oxygen constituents [O, O_2, and O_3] and (2) electron-ion recombination rates, dependent upon the positive ion composition. At lower altitudes where the ratio of negative ions to electrons (λ) is much greater than 1, electron recovery is initially dominated by the faster attachment processes. At higher altitudes where λ approaches unity or at lower altitudes after detachment processes have balanced attachment processes, electron recovery is controlled by the slower electron-ion recombination processes. For ionospheric disturbances produced by electric field

changes from lightning discharges, the recovery rates of the electron density enhancements will thereby depend significantly upon conditions at the altitudes where the electric breakdown occurs.

The observed VLF scattering results from the differential scattering integrated throughout the entire disturbance geometry [e.g., see *Wait*, 1964, equation 14]. Consequently, the recovery dynamics of the observed scattered field depend upon the recovery of the disturbance geometry [e.g., *Nunn and Rodger*, 1999]. Note that when the electron density enhancements are large enough such that the first-order Born approximation does not hold, the scattered field will not be linearly proportional to changes in the electron density profile. In this context, the model results can now be used to explain the occurrence of both typical and long recovery VLF scattering events.

Typical recovery VLF events occur when electron density enhancements at lower altitudes are quickly lost due to fast attachment processes (e.g., Figure 3, $\leq$77 km, $E_o \leq 3E_k$), and electron density enhancements at higher altitudes are too small to produce observable scattering beyond typical recovery timescales (e.g., Figure 3., $\geq$78 km, $E_o \leq 2E_k$). Consequently, the observed scattered field in typical recovery events is dominated by scattering from the regions where electron loss is sufficiently controlled by fast attachment.

Long recovery VLF events occur when electron density enhancements controlled by slow recombination processes are large enough to produce observable scattering for >300 s. Consequently, long recovery scattering may necessitate efficient, long recovery differential scattering over relatively large areas. Efficient, long recovery differential scattering can occur at lower altitudes for large electron density enhancements that persist after attachment losses are balanced by detachment gains (e.g., Figure 3, 76 km, $E_o = 5E_k$) and at higher altitudes for large electron density enhancements (e.g., Figure 3, $\geq$78 km, $E_o \geq 3E_k$). The large electron density enhancements required to reproduce LORE recovery times are consistent with both the association of LOREs with high peak current lightning flashes [e.g., *Haldoupis et al.*, 2013; *Salut et al.*, 2013] and the relative rarity of LORE observations.

No appreciable difference in electron recovery was found for electric field pulses of different time widths (up to $2\Delta t = 1$ ms) which produced approximately the same initial electron density enhancement. Consequently, our modeling results and the LORE mechanisms identified are indifferent to the specific source of the electric field change (e.g., radiation versus quasi-electrostatic) and may be associated with a variety of different TLEs. The recovery mechanisms of electron density enhancements discussed in this work should also apply to transient disturbances of the lower ionosphere produced by a variety of other geophysical phenomena (e.g., solar flares, solar proton events, and lightning-induced electron precipitation).

In response to the changing geometry of the electron density disturbance during recovery, it is likely that the VLF scattering pattern will change with time. Simultaneous and multiple ground-based observations of a VLF scattering event can be used to measure scattering patterns, from which the horizontal disturbance geometry can be inferred [e.g., *Johnson et al.*, 1999a, 1999b; *Moore et al.*, 2003]. Consequently, the spatiotemporal dynamics of large ionization events could be inferred from antenna array measurements of long recovery VLF scattering events. Knowledge of the spatiotemporal dynamics of ionospheric disturbances, coupled with the understanding of their recovery mechanisms, might allow experimenters to infer information regarding the ionization source and its distribution. We note, however, that accurate measurements of scattered field recoveries can be difficult due to natural ionospheric variations which can occur on timescales of minutes (see discussion in *Dowden et al.* [2001]).

Additionally, subtle variations in the frequency dependence of the VLF scattering process (e.g., see Figure 3) could provide information regarding both the horizontal and vertical profiles of the disturbance, but the frequency dependence of propagation effects would also need to be accounted for. Furthermore, the various waveguide modes which comprise the VLF radio wave might exhibit different susceptibilities to scattering. *Wait* [1964] showed that scattering can be calculated in terms of the change in eigenangle solutions within the disturbed ionospheric region, and *Poulsen et al.* [1993] showed that within ionospheric disturbances the various modes can exhibit different changes in their respective eigenangle solution. Consequently, it is not unreasonable that scattering time dynamics might vary among the various propagating waveguide modes. Experiments which could determine the modal content of subionospherically propagating VLF waves might then provide important additional information regarding the spatiotemporal dynamics of the ionospheric disturbance.

Acknowledgments
This work is supported by DARPA and the U.S. Air Force through contract FA8650-15-C-7535 to the University of Florida. The authors would like to thank Martin A. Uman for his helpful comments on the manuscript. Data utilized in this paper, including the NRLMSISE-00 neutral constituency and temperature, are available upon request by contacting R.C. Moore (moore@ece.ufl.edu).

References

Allen, M., J. I. Lunine, and Y. L. Yung (1984), The vertical distribution of ozone in the mesosphere and lower thermosphere, *J. Geophys. Res.*, *89*(D3), 4841–4872.
Arnold, F., D. Krankowsky, E. Zettwitz, and W. Joos (1980), Strong temperature control of the ionospheric D-region: Evidence from in situ ion composition measurements, *J. Atmos. Terr. Phys.*, *42*, 249–256.
Brasseur, G. P., and S. Solomon (2005), *Aeronomy of the Middle Atmosphere*, 3rd ed., Springer, Dordrecht, Netherlands.
Cheng, Z., S. A. Cummer, H.-T. Su, and R.-R. Hsu (2007), Broadband very low frequency measurement of D region ionospheric perturbations caused by lightning electromagnetic pulses, *J. Geophys. Res.*, *112*, A06318, doi:10.1029/2006JA011840.
Cotts, B. R. T., and U. S. Inan (2007), VLF observation of long ionospheric recovery events, *Geophys. Res. Lett.*, *34*, L14809, doi:10.1029/2007GL030094.
Dowden, R. L., J. B. Brundell, and C. J. Rodger (1997), Temporal evolution of very strong Trimpis observed at Darwin, Australia, *Geophys. Res. Lett.*, *24*(19), 2419–2422.
Dowden, R., C. Rodger, J. Brundell, and M. Clilverd (2001), Decay of whistler-induced electron precipitation and cloud-ionosphere electrical discharge Trimpis: Observations and analysis, *Radio Sci.*, *1*, 151–169.
Enell, C.-F., et al. (2008), Parameterisation of the chemical effects of sprites in the middle atmosphere, *Ann. Geophys.*, *26*, 13–27.
Gluhkov, V. S., V. P. Pasko, and U. S. Inan (1992), Relaxation of transient lower ionospheric disturbances caused by lightning-whistler-induced electron precipitation bursts, *J. Geophys. Res.*, *97*(A11), 16,971–16,979.
Gordillo-Vázquez, F. J. (2008), Air plasma kinetics under the influence of sprites, *J. Phys. D*, *41*, 234016.
Gordillo-Vázquez, F. J. (2010), Vibrational kinetics of air plasmas induced by sprites, *J. Geohys. Res.*, *115*, A00E25, doi:10.1029/2009JA014688.
Gordillo-Vázquez, F. J., and A. Luque (2010), Electrical conductivity in sprite streamer channels, *Geophys. Res. Lett.*, *37*, L16809, doi:10.1029/2010GL044349.
Haldoupis, C., R. J. Steiner, Á. Mika, S. Shalimov, R. A. Marshall, U. S. Inan, T. Bösinger, and T. Neubert (2006), 'Early/slow" events: A new category of VLF perturbations observed in relation with sprites, *J. Geophys. Res.*, *111*, A11321, doi:10.1029/2006JA011960.
Haldoupis, C., Á. Mika, and S. Shalimov (2009), Modeling the relaxation of early VLF perturbations associated with transient luminous events, *J. Geophys. Res.*, *114*, A00E04, doi:10.1029/2009JA014313.
Haldoupis, C., N. Amvrosiadi, B. R. T. Cotts, O. A. van der Velde, O. Chanrion, and T. Neubert (2010), More evidence for a one-to-one correlation between Sprites and Early VLF perturbations, *J. Geophys. Res.*, *115*, A07304, doi:10.1029/2009JA015165.
Haldoupis, C., M. Cohen, B. Cotts, E. Arnone, and U. Inan (2012), Long-lasting D-region ionospheric modifications, caused by intense lightning in association with elve and sprite pairs, *Geophys. Res. Lett.*, *39*, L16801, doi:10.1029/2012GL052765.
Haldoupis, C., M. Cohen, E. Arnone, B. Cotts, and S. Dietrich (2013), The VLF fingerprint of elves: Step-like and long-recovery early VLF perturbations caused by powerful ±CG lightning EM pulses, *J. Geophys. Res. Space Physics*, *118*, 5392–5402, doi:10.1002/jgra.50489.
Han, F., and S. A. Cummer (2010), Midlatitude nighttime D region ionosphere variability on hourly to monthly time scales, *J. Geophys. Res.*, *115*, A09323, doi:10.1029/2010JA015437.
Hardman, S. F., C. J. Rodger, R. L. Dowden, and J. B. Brundell (1998), Measurements of the VLF scattering pattern of the structured plasma of red sprites, *IEEE Antennas Propag. Mag.*, *40*(2), 29–38.
Heaps, M. G. (1978), Parametrization of the cosmic ray ion-pair production rate above 18 km, *Planet. Space Sci.*, *26*, 513–517.
Inan, U. S., A. Slingeland, and V. P. Pasko (1996), VLF and LF signatures of mesospheric/lower ionospheric response to lightning discharges, *J. Geophys. Res.*, *101*(A3), 5219–5238.
Johnson, M. P., U. S. Inan, S. J. Lev-Tov, and T. F. Bell (1999a), Scattering pattern of lightning-induced ionospheric disturbances associated with early/fast VLF events, *Geophys. Res. Lett.*, *26*(15), 2363–2366.
Johnson, M. P., U. S. Inan, and D. S. Lauben (1999b), Subionospheric VLF signatures of oblique (nonducted) whistler-induced precipitation, *Geophys. Res. Lett.*, *26*(23), 3569–3572.
Lehtinen, N. G., and U. S. Inan (2007), Possible persistent ionization caused by giant blue jets, *Geophys. Res. Lett.*, *34*, L08804, doi:10.1029/2006GL029051.
Liu, N. (2012), Multiple ion species fluid modeling of sprite halos and the role of electron detachment of O^- in their dynamics, *J. Geophys. Res.*, *117*, A03308, doi:10.1029/2011JA017062.
Marshall, R. A., U. S. Inan, and W. A. Lyons (2006), On the association of early/fast very low frequency perturbations with sprites and rare examples of VLF backscatter, *J. Geophys. Res.*, *111*, D19108, doi:10.1029/2006JD007219.
Marshall, R. A., T. Adachi, R.-R. Hsu, and A. B. Chen (2014), Rare examples of early VLF events observed in association with ISUAL-detected gigantic jets, *Radio Sci.*, *49*, 36–43, doi:10.1002/2013RS005288.
Meier, R. R. (1969), Balmer alpha and Lyman beta in the hydrogen geocorona, *J. Geophys. Res.*, *74*(14), 3651–3574.
Meier, R. R., and P. Mange (1973), Spatial and temporal variations of the Lyman-alpha airglow and related atomic hydrogen distributions, *Planet. Space. Sci.*, *21*, 309–327.
Mitra, A. P. (1975), D-region in disturbed conditions, including flares and energetic particles, *J. Atmos. Terr. Phys.*, *37*, 895–913.
Miyasato, R., H. Fukunishi, Y. Takahashi, and M. J. Taylor (2003), Energy estimation of electrons producing sprite halos using array photometer data, *J. Atmos. Sol. Terr. Phys.*, *65*, 573–581.
Moore, R. C., C. P. Barrington-Leigh, U. S. Inan, and T. F. Bell (2003), Early/fast VLF events produced by electron density changes associated with sprite halos, *J. Geophys. Res.*, *108*(A10), 1363, doi:10.1029/2002JA009816.
Nunn, D., and C. J. Rodger (1999), Modeling the relaxation of red sprite plasma, *Geophys. Res. Lett.*, *26*(21), 3293–3296.
Ogawa, T., and T. Shimazaki (1975), Diurnal variations of odd nitrogen and ionic densities in the mesosphere and lower thermosphere: Simultaneous solution of the photochemical-diffusive equations, *J. Geophys. Res.*, *80*(28), 3945–3960.
Pasko, V. P., and U. S. Inan (1994), Recovery signatures of lightning-associated VLF perturbations as a measure of the lower ionosphere, *J. Geophys. Res.*, *99*(A9), 17,523–17,537.
Picone, J. M., A. E. Hedin, D. P. Drob, and A. C. Aikin (2002), NRLMSISE-00 empirical model of the atmosphere: Statistical comparisons and scientific issues, *J. Geophys. Res.*, *107*(A12), 1468, doi:10.1029/2002JA009430.
Poulsen, W. L., U. S. Inan, and T. F. Bell (1993), A multiple-mode three-dimensional model of VLF propagation in the Earth-ionosphere waveguide in the presence of localized D region disturbances, *J. Geophys. Res.*, *98*(A2), 1705–1717.
Rapp, D., P. E. Golden, and D. D. Briglia (1965), Cross sections for dissociative ionization of molecules by electron impact, *J. Chem. Phys.*, *42*(12), 4081–4085.
Ratcliffe, J. A. (1959), *The Magneto-Ionic Theory and Its Applications to the Ionosphere*, Cambridge Univ. Press, Cambridge, U. K.
Reid, G. C. (1977), The production of water-cluster positive ions in the quiet daytime D region, *Planet. Space Sci.*, *25*, 275–290.
Rodger, C. J. (2003), Subionospheric VLF perturbations associated with lightning discharges, *J. Atmos. Sol. Terr. Phys.*, *65*, 591–606.

Rodger, C. J., M. Cho, M. A. Clilverd, and M. J. Rycroft (2001), Lower ionospheric modification by lightning-EMP: Simulation of the night ionosphere over the United States, *Geophys. Res. Lett.*, *28*(2), 199–202.

Rowe, J. N., A. P. Mitra, A. J. Ferraro, and H. S. Lee (1974), An experimental and theoretical study of the D-region—II. A semi-empirical model for mid-latitude D-region, *J. Atmos. Terr. Phys.*, *36*, 755–785.

Salut, M. M., M. B. Cohen, M. A. M. Ali, K. L. Graf, B. R. T. Cotts, and S. Kumar (2013), On the relationship between lightning peak current and Early VLF perturbations, *J. Geophys. Res. Space Physics*, *118*, 7272–7282, doi:10.1002/2013JA019087.

Sampath, H. T., U. S. Inan, and M. P. Johnson (2000), Recovery signatures and occurrence properties of lightning-associated subionospheric VLF perturbations, *J. Geophys. Res.*, *105*(A1), 183–191.

Sentman, D. D., H. C. Stenbaek-Nielsen, M. G. McHarg, and J. S. Morrill (2008), Plasma chemistry of sprite streamers, *J. Geophys. Res.*, *113*, D11112, doi:10.1029/2007JD008941.

Smith, D., and M. J. Church (1977), Ion-ion recombination rates in Earth's atmosphere, *Planet. Space Sci.*, *25*, 433–439.

Strobel, D. F., D. M. Hunten, and M. B. McElroy (1970), Production and diffusion of nitric oxide, *J. Geophys. Res.*, *75*(22), 4307–4321.

Thomas, L., and M. R. Bowman (1985), Model studies of the D-region negative-ion composition during day-time and night-time, *J. Atmos. Terr. Phys.*, *47*(6), 546–556.

Thomson, N. R., and W. M. McRae (2009), Nighttime ionospheric D region: Equatorial and nonequatorial, *J. Geophys. Res.*, *114*, A08305, doi:10.1029/2008JA014001.

Thomson, N. R., M. A. Clilverd, and W. M. McRae (2007), Nighttime ionospheric *D* region parameters from VLF phase and amplitude, *J. Geophys. Res.*, *112*, A07304, doi:10.1029/2007JA012271.

Wait, J. R. (1964), On phase changes in very-low-frequency propagation induced by an ionospheric depression of finite extent, *J. Geophys. Res.*, *69*(3), 441–445.

Wait, J. R., and K. P. Spies (1964), Characteristics of the Earth-ionosphere waveguide for VLF radio waves, Tech. Note 300, Nat. Bureau of Standards.

Watanabe, K. (1958), Ultraviolet absorption processes in the upper atmosphere, *Adv. Geophys.*, *5*, 153–221.

Whitten, R. C., and I. G. Poppoff (1965), *Physics of the Lower Ionosphere*, Prentice-Hall, Englewood Cliffs, N. J.